

Here, for the TBL:

$$H_0(\theta) = H_0^{(\text{Lieb})}(\theta) = t((\tilde{q}_x)\lambda_2 + (\tilde{q}_y)\lambda_7) + t_2q^2, \quad (2)$$

where $\tilde{q}_x \equiv q_x \cos(\theta) - q_y \sin(\theta)$, $\tilde{q}_y \equiv q_x \sin(\theta) + q_y \cos(\theta)$, and $\vec{q} = \vec{k} - \vec{k}_M^{(\theta)}$ with $\vec{k}_M^{(\theta)}$ be the k -vector of the M valley in the *rotated* monolayer Brillouin zone (FIG. 2(a)). The $\{\lambda_i\}$ are Gellmann matrices [27]. On the other hand, for the TBD:

$$H_0(\theta) = H_0^{(\text{Dice})}(\theta, \zeta) = \frac{3t}{2}(\zeta q_x \hat{x} - q_y \hat{y}) \cdot \vec{S}^{(\theta)} + t_2q^2, \quad (3)$$

where $\vec{S}^{(\theta)} \equiv e^{-i\frac{\theta}{2}S_3} \vec{S} e^{i\frac{\theta}{2}S_3}$ and $\zeta = \pm$ indicates the valley degree of freedom. The vector $\vec{q} = \vec{k} - K_\zeta^{(\theta)}$ with $K_\zeta^{(\theta)}$ be the K_ζ valley in the *rotated* monolayer BZ of Dice lattice (FIG. 2(b)). The $\{S_i\}$ are matrix representations of spin-1 in the basis of s_z eigenstates [28]. Note that the basis in Eqs. 2 and 3 is $(A, B, C)^T$, where A, B , and C are sublattices in the monolayer lattices (FIG. 1).

The interlayer coupling T has the following form [26, 29]:

$$T = \begin{pmatrix} \omega_1 g(\vec{r}) & \omega_2 g(\vec{r} - \vec{r}_{12}) & \omega_3 g(\vec{r} - \vec{r}_{13}) \\ \omega_2 g(\vec{r} + \vec{r}_{12}) & \omega_1 g(\vec{r}) & \omega_2 g(\vec{r} - \vec{r}_{23}) \\ \omega_3 g(\vec{r} + \vec{r}_{13}) & \omega_2 g(\vec{r} + \vec{r}_{23}) & \omega_1 g(\vec{r}) \end{pmatrix}, \quad (4)$$

where $g(\vec{r}) = \sum_i e^{i\vec{q}_i \cdot \vec{r}}$ with \vec{q}_i representing the momentum transfer of interlayer tunneling between valleys from different layers in the Moiré Brillouin zone (Figs. 2(a) and 2(b)). For TBL, $\vec{q}_1 = \frac{\pi}{L_s} \hat{x} + \frac{\pi}{L_s} \hat{y}$, $\vec{q}_2 = -\frac{\pi}{L_s} \hat{x} + \frac{\pi}{L_s} \hat{y}$, $\vec{q}_3 = \frac{\pi}{L_s} \hat{x} - \frac{\pi}{L_s} \hat{y}$, and $\vec{q}_4 = -\frac{\pi}{L_s} \hat{x} - \frac{\pi}{L_s} \hat{y}$. For TBD, $\vec{q}_1 = -\frac{4\pi}{3L_s} \hat{y}$, $\vec{q}_2 = \frac{2\pi}{\sqrt{3}L_s} \hat{x} + \frac{2\pi}{3L_s} \hat{y}$, $\vec{q}_3 = -\frac{2\pi}{\sqrt{3}L_s} \hat{x} + \frac{2\pi}{3L_s} \hat{y}$. In Eq. 4, \vec{r}_{ij} represents the center of different stacked regions in the Moiré unit cell, and the origin of the coordinates is set at the center of the AA-stacked region, see Supplementary Material for details of lattice geometry of high-symmetry stacking. For the TBL, positions of different stacked regions are $\vec{r}_{12} = \vec{r}_{AB_x} = \frac{L_s}{2} \hat{y}$, $\vec{r}_{23} = \vec{r}_{AB_y} = \frac{L_s}{2} \hat{x}$, and $\vec{r}_{13} = \vec{r}_{AB_{xy}} = \frac{L_s}{2} (\hat{x} + \hat{y})$ (see FIG. 1(a)). For the TBD, positions of different stacked regions are $\vec{r}_{12} = \vec{r}_{23} = -\vec{r}_{13} = \vec{r}_{AB} = \frac{L_s}{\sqrt{3}} \hat{x}$ (FIG. 1(b)).

Electronic structure of twisted bilayers.— The band structures obtained from diagonalizing Eq. 1 in the plane-wave basis are shown in FIG. 3(a.) for TBL and FIG. 4(a.) for TBD, which show isolated flat bands at the band edge around the Fermi level. These isolated flat bands are generated by gapping the folded parabolic dispersion originating from the second nearest-neighbor hopping through the interlayer tunneling ω_1 . To demonstrate this fact and get more insight into the TBL and TBD, let's consider the case where $\omega_1 = \omega_3 = t_2 = 0$. In this scenario, the electrons hop only between the A, B sublattice and A, C sublattice in both layers, which keeps the twisted bilayer lattice bipartite [1–3], making the

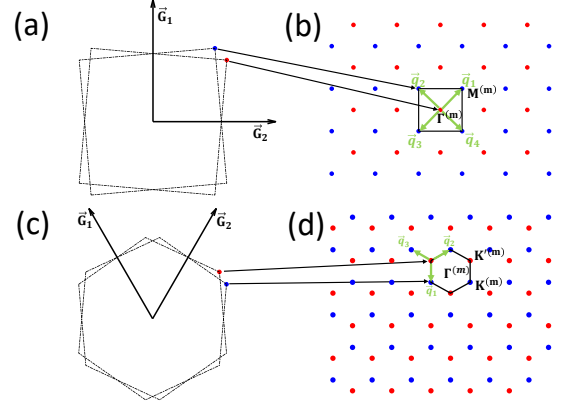


FIG. 2. (a) BZ of the Lieb lattice on the top (blue) and bottom (red) layer. \vec{G}_i are the reciprocal lattice vectors for an unrotated monolayer Lieb lattice. (b) Moiré BZ of the TBL. The M -points of the top layer (blue) and of the bottom layer (red) map to the $M^{(m)}$ point and the $\Gamma^{(m)}$ point in the Moiré Brillouin zone, respectively. (c) The Brillouin zone of the Dice lattice on the top (blue) and bottom (red) layer. The \vec{G}_i indicates the reciprocal lattice vectors of an unrotated monolayer Dice lattice. (d) The Moiré Brillouin zone of the TBD system. The K -points of the top layer (blue) and of the bottom layer (red) map to the $K'^{(m)}$ point and the $K^{(m)}$ point in the Moiré Brillouin zone, respectively.

Hamiltonian in Eq. 1 non-invertible and, therefore, hosting robust zero-energy states [30]. When $t_2 = 0$, the existence of flat bands poses a challenge in validating Moiré band structure calculations using low-energy continuum models.

To properly describe the TBL and TBD when $t_2 = 0$, we construct the tight-binding model with Slater-Koster parameterization. The setting $\omega_1 = \omega_3 = 0$ corresponds to no interlayer tunneling between the same sublattice on different layers and no interlayer tunneling from A and C sublattices on different layers. When second-nearest neighbor hopping is not considered, the vanishing ω_1 and ω_3 leads to isolated exact flat bands at $E = 0$ with considerable degeneracies in the Moiré Brillouin zone (see FIG. 3(b.) and FIG. 4(b.)). In this scenario, the system is controlled by the parameter $\alpha \equiv \frac{\omega_2}{tk_F}$. Due to the special hopping structure in TBD and TBL when $\omega_1 = \omega_3 = t_2 = 0$, the number of these flat bands is $\frac{1}{3}$ of the total bands. Remarkably, these flat bands remain isolated for a large range of α as shown in FIG. 5(a.) and FIG. 5(b.).

Due to the time-reversal symmetry, these isolated flat bands have no net Chern numbers. The Wilson loop calculation also shows that the isolated flat bands in TBL and TBD do not have non-trivial winding of the hybridized Wannier centers (see FIG. 6(a.) and FIG. 6(b.)). Due to the time-reversal symmetry, the flat bands in the TBL have no Berry curvature around

its M valley. In contrast, the flat bands in the TBD are found to host considerable Berry curvature around the K, K' valleys (see FIG. 6(c.)). Note that the Berry curvature around each valley doesn't give a non-trivial valley Chern number, which is consistent with the analysis from the pseudo-Landau level representation of the isolated flat bands in TBD [29]. More specifically, due to the bipartite nature, the pseudo-Landau level spectrum has $\frac{1}{3}$ total number of Landau levels are zero modes. However, we find that the zero-mode of the $n = 0$ pseudo-Landau level cancels out the contribution of the Hall conductivity from the zero-modes of $n \neq 0$ pseudo-Landau level (see Supplementary Material). In contrast to twisted bilayer graphene, the zero-mode generated by $n = 0$ Landau levels in TBD do not contribute an integer conductivity quanta, and the zero-modes of the pseudo-Landau level in TBD are also generated by $n \neq 0$ Landau levels, which makes the zero-modes of pseudo-Landau levels contribute no net Chern number.

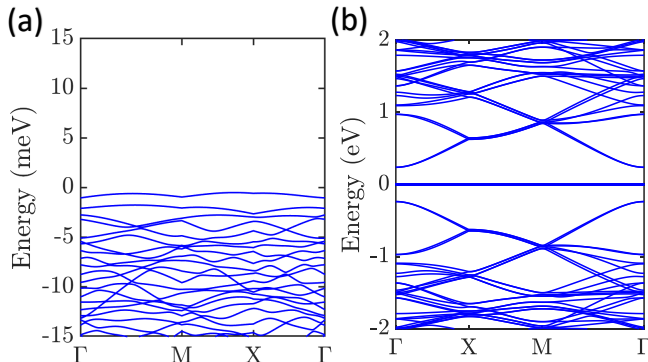


FIG. 3. (a) The band structure of the Hamiltonian in Eq. 1 for TBL with $\alpha \cong 1.423$, in which $t = 5.817$ eV, $t_2 = -0.1$ eV, $\omega_1 = -0.001$ eV, $\omega_2 \cong 1.163$ eV, and $\omega_3 = 0$. (b) The band structure of the TBL generated by the tight-binding model with Slater-Koster parameterization, which corresponds to the continuum model in Eq. 1 with $\alpha \cong 1.423$ and $t_2 = \omega_1 = \omega_3 = 0$.

Discussion— In contrast to prior twisted materials where the count of low-energy flat bands remains constant with varying twisted angles, the twisted bilayer Lieb (TBL) and Dice (TBD) lattices exhibit a twist angle-dependent quantity of flat bands near the Fermi level. Notably, these quantities increase at a rate greater than $\frac{1}{\varrho^2}$ as the twist angle θ decreases (FIG. 7).

The introduction of second nearest-neighbor (SNN) hopping t_2 and chiral-symmetry-breaking tunneling terms ω_1 or ω_3 disrupts the bipartite nature of the Moiré lattice structure, resulting in the coupling of these flat bands. However, as long as these effects are not overly significant, the cluster of flat bands near the Fermi level

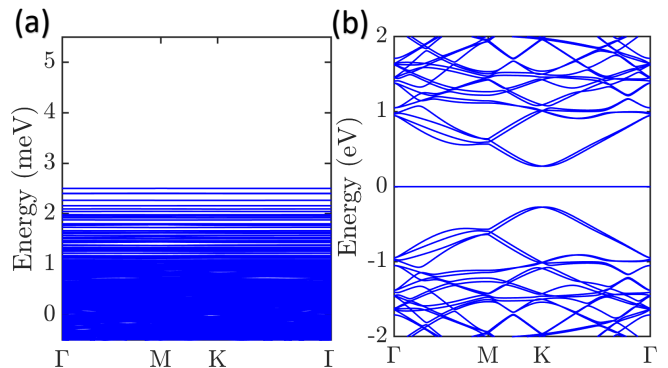


FIG. 4. (a) The band structure of the Hamiltonian in Eq. 1 for TBD with $\alpha \cong 19.429$, in which $t = 5.817$ eV, $t_2 = -0.1$ eV, $\omega_1 = 0.001$ eV, $\omega_2 \cong 1.163426$ eV, and $\omega_3 = 0$ eV. (b) The band structure of the TBD generated by the tight-binding model with Slater-Koster parameterization, which corresponds to the continuum model in Eq. 1 with $\alpha \cong 19.429$ and $t_2 = \omega_1 = \omega_3 = 0$.

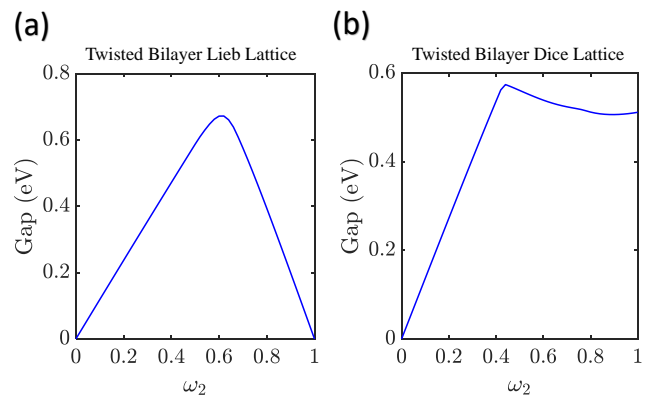


FIG. 5. (a) The gap between the flat bands and other high-energy bands in the tight-binding model of TBL with $t_2 = \omega_1 = \omega_3 = 0$ as a function of interlayer tunneling ω_2 . (b) The gap between the flat bands and the high-energy bands in the tight-binding model of TBD with $t_2 = \omega_1 = \omega_3 = 0$ as a function of interlayer tunneling ω_2 .

remains isolated from the high-energy spectra. Specifically, the consideration of SNN hopping t_2 leads to a parabolic dispersion of the flat bands near the valleys. Meanwhile, the inclusion of ω_1 acts as an interaction, opening a gap in the parabolic dispersion and creating isolated flat bands at the upper band edge of the flat band cluster. In this scenario, the system is governed by three key parameters: $\alpha \equiv \frac{\omega_2}{tk_\theta}$, $\beta \equiv \frac{t_2}{tk_\theta}$, and $\gamma \equiv \frac{\omega_1}{tk_\theta}$. A similar effect is expected with the inclusion of ω_3 . Further exploration of the topological phase diagram concerning α , β , and γ will be interesting.

It is noteworthy that the twisted bilayer Dice lattice

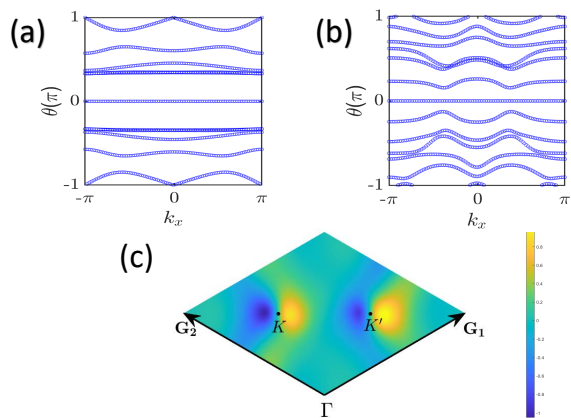


FIG. 6. (a) The hybridized Wannier center of the isolated flat bands in TBL. (b) The hybridized Wannier center of the isolated flat bands in TBD. (c) The Berry curvature generated by the isolated flat bands of the TBD at $\alpha \cong 19.429$ in the Moiré Brillouin zone, which is concentrated around the valleys.

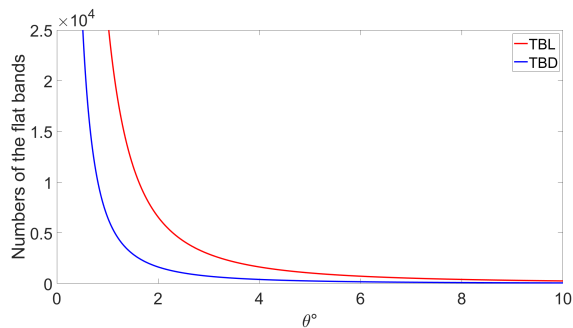


FIG. 7. The number of flat bands in TBL and TBD as a function of twisting angle θ . When θ is small, the number of sublattice sites in the Moiré unit cell of TBL $N_{\text{sites}}^{(\text{TBL})} \sim 6 \csc^2(\frac{\theta}{2})$ [31] and the number of flat bands in the Moiré unit cell of TBD $N_{\text{sites}}^{(\text{TBD})} \sim \frac{3}{1-\cos(\theta)}$ [32]. The corresponding number of flat bands in TBL is $N_{\text{flat}}^{(\text{TBL})} = \frac{1}{3}N_{\text{sites}}^{(\text{TBL})}$ and in TBD is $N_{\text{flat}}^{(\text{TBD})} = \frac{1}{3}N_{\text{sites}}^{(\text{TBD})}$.

(TBD) exhibits a valley structure characterized by a concentrated Berry curvature, signifying a substantial quantum weight. Consequently, upon introducing a BCS-type pairing potential, this leads to a noteworthy superfluid weight [33–35]. Moreover, the dramatic variation in the density of states (DOS) with respect to the twist angle suggests a promising way for the realization of tuning the transition temperature by adjusting the twist angle. As the number of flat bands increases with a decrease in the twist angle, it is anticipated that the transition temperature will increase at a smaller twist angle due to the

growing DOS [36]. This paves the way toward controllable high-temperature superconductivity.

The count of flat bands near the Fermi level undergoes a dramatic change with varying twist angles, especially noticeable at small angles. Therefore, Moiré engineering of the TBL and TBD offers an exceptional platform for investigating strongly correlated physics, in which a slight tweak in the twist angle can exert a large influence on low-energy physics. For instance, manipulating the twist angle allows for engineering spontaneous ferromagnetic phase transitions based on the Stoner criterion. This is achieved by inducing dramatic changes in the DOS near the Fermi level, considering the spin degree of freedom through significant spin-orbit coupling or the presence of magnetic impurities [36]. Notably, the TBL and TBD exemplify how Moiré engineering paves a novel pathway for manipulating geometry-induced flat bands in bipartite lattices.

The Moiré pattern provides not only an alternative way, distinct from dimerization or anisotropic strain, to isolate flat bands in bipartite lattices but also enables the creation of a large supercell, folding numerous flat bands into the first Brillouin zone. Additionally, while inheriting flat band physics from the unrotated monolayer, the Moiré pattern generates a distinctive electronic structure characterized by highly degenerate flat bands near the Fermi level. Further investigation into strongly correlated physics and the corresponding phase diagram within the realm of twisted bipartite lattices will be interesting.

ACKNOWLEDGEMENTS

We thank Gregory Fiete for the discussions. The work was supported by the Air Force Office of Scientific Research under award number FA9550-20-1-0322 and benefited from the computational resources of Northeastern University’s Advanced Scientific Computation Center (ASCC) and the Discovery Cluster.

Note: After the completion of our manuscript, we became aware of the related paper [37].

* X. Z., Y. H., and B. W. contributed equally to this work.; x.zhou@northeastern.edu

† X. Z., Y. H., and B. W. contributed equally to this work.

‡ ar.bansil@northeastern.edu

- [1] B. Sutherland, Localization of electronic wave functions due to local topology, *Phys. Rev. B* **34**, 5208 (1986).
- [2] D. Călugăru, A. Chew, L. Elcoro, Y. Xu, N. Regnault, Z.-D. Song, and B. A. Bernevig, General construction and topological classification of crystalline flat bands, *Nature Physics* **18**, 185 (2022).

- [3] F. Wang and H. Zhang, Flat bands and magnetism in Fe_4GeTe_2 and Fe_5GeTe_2 due to bipartite crystal lattices (2023), arXiv:2306.15996 [cond-mat.mtrl-sci].
- [4] A. Mielke, Ferromagnetism in the hubbard model on line graphs and further considerations, *Journal of Physics A: Mathematical and General* **24**, 3311 (1991).
- [5] A. Mielke, Ferromagnetic ground states for the hubbard model on line graphs, *Journal of Physics A: Mathematical and General* **24**, L73 (1991).
- [6] H. Mielke A., Tasaki, Ferromagnetism in the hubbard model, *Commun. Math. Phys.* **158**, 341 (1993).
- [7] I. Syôzi, Statistics of Kagomé Lattice, *Progress of Theoretical Physics* **6**, 306 (1951), <https://academic.oup.com/ptp/article-pdf/6/3/306/5239621/6-3-306.pdf>.
- [8] E. H. Lieb, Two theorems on the hubbard model, *Phys. Rev. Lett.* **62**, 1201 (1989).
- [9] J. Sun, T. Liu, Y. Du, and H. Guo, Strain-induced pseudo magnetic field in the $\alpha - T_3$ lattice, *Phys. Rev. B* **106**, 155417 (2022).
- [10] W. Jiang, M. Kang, H. Huang, H. Xu, T. Low, and F. Liu, Topological band evolution between lieb and kagome lattices, *Phys. Rev. B* **99**, 125131 (2019).
- [11] L.-K. Lim, J.-N. Fuchs, F. Piéchon, and G. Montambaux, Dirac points emerging from flat bands in lieb-kagome lattices, *Phys. Rev. B* **101**, 045131 (2020).
- [12] S. Mondal and S. Basu, Topological features of the haldane model on a dice lattice: Flat-band effect on transport properties, *Phys. Rev. B* **107**, 035421 (2023).
- [13] E. V. Gorbar, V. P. Gusynin, and D. O. Oriekhov, Electron states for gapped pseudospin-1 fermions in the field of a charged impurity, *Phys. Rev. B* **99**, 155124 (2019).
- [14] P. O. Sukhachov, D. O. Oriekhov, and E. V. Gorbar, Stackings and effective models of bilayer dice lattices, *Phys. Rev. B* **108**, 075166 (2023).
- [15] P. O. Sukhachov, D. O. Oriekhov, and E. V. Gorbar, Optical conductivity of bilayer dice lattices, *Phys. Rev. B* **108**, 075167 (2023).
- [16] S. Okamoto and D. Xiao, Transition-metal oxide (111) bilayers, *Journal of the Physical Society of Japan* **87**, 041006 (2018), <https://doi.org/10.7566/JPSJ.87.041006>.
- [17] D. Doennig, W. E. Pickett, and R. Pentcheva, Massive symmetry breaking in $\text{LaAlO}_3/\text{SrTiO}_3$ (111) quantum wells: A three-orbital strongly correlated generalization of graphene, *Phys. Rev. Lett.* **111**, 126804 (2013).
- [18] R. Soni, N. Kaushal, S. Okamoto, and E. Dagotto, Flat bands and ferrimagnetic order in electronically correlated dice-lattice ribbons, *Phys. Rev. B* **102**, 045105 (2020).
- [19] G. Tarnopolsky, A. J. Kruchkov, and A. Vishwanath, Origin of magic angles in twisted bilayer graphene, *Phys. Rev. Lett.* **122**, 106405 (2019).
- [20] Z. Song, Z. Wang, W. Shi, G. Li, C. Fang, and B. A. Bernevig, All magic angles in twisted bilayer graphene are topological, *Phys. Rev. Lett.* **123**, 036401 (2019).
- [21] A. Parhizkar and V. Galitski, A generic topological criterion for flat bands in two dimensions (2023), arXiv:2301.00824 [cond-mat.mes-hall].
- [22] T. Devakul, V. Crépel, Y. Zhang, and L. Fu, Magic in twisted transition metal dichalcogenide bilayers, *Nature Communications* **12**, 6730 (2021).
- [23] Y. Cao, V. Fatemi, S. Fang, K. Watanabe, T. Taniguchi, E. Kaxiras, and P. Jarillo-Herrero, Unconventional superconductivity in magic-angle graphene superlattices, *Nature* **556**, 43 (2018).
- [24] M. Yankowitz, S. Chen, H. Polshyn, Y. Zhang, K. Watanabe, T. Taniguchi, D. Graf, A. F. Young, and C. R. Dean, Tuning superconductivity in twisted bilayer graphene, *Science* **363**, 1059 (2019), <https://www.science.org/doi/pdf/10.1126/science.aav1910>.
- [25] F. Wu, T. Lovorn, E. Tutuc, I. Martin, and A. H. MacDonald, Topological insulators in twisted transition metal dichalcogenide homobilayers, *Phys. Rev. Lett.* **122**, 086402 (2019).
- [26] R. Bistritzer and A. H. MacDonald, Moiré bands in twisted double-layer graphene, *Proceedings of the National Academy of Sciences* **108**, 12233 (2011), <https://www.pnas.org/doi/pdf/10.1073/pnas.1108174108>.
- [27] The gellmann matrices in this letter are: $\lambda_1 = \begin{pmatrix} 0 & 1 & 0 \\ 1 & 0 & 0 \\ 0 & 0 & 0 \end{pmatrix}$, $\lambda_2 = \begin{pmatrix} 0 & -i & 0 \\ i & 0 & 0 \\ 0 & 0 & 0 \end{pmatrix}$, $\lambda_3 = \begin{pmatrix} 1 & 0 & 0 \\ 0 & -1 & 0 \\ 0 & 0 & 0 \end{pmatrix}$, $\lambda_4 = \begin{pmatrix} 0 & 0 & 1 \\ 0 & 0 & 0 \\ 1 & 0 & 0 \end{pmatrix}$, $\lambda_5 = \begin{pmatrix} 0 & 0 & -i \\ 0 & 0 & 0 \\ i & 0 & 0 \end{pmatrix}$, $\lambda_6 = \begin{pmatrix} 0 & 0 & 0 \\ 0 & 0 & 1 \\ 0 & 1 & 0 \end{pmatrix}$, $\lambda_7 = \begin{pmatrix} 0 & 0 & 0 \\ 0 & 0 & -i \\ 0 & i & 0 \end{pmatrix}$, $\lambda_8 = \frac{1}{\sqrt{3}} \begin{pmatrix} 1 & 0 & 0 \\ 0 & 1 & 0 \\ 0 & 0 & -2 \end{pmatrix}$.
- [28] The spin matrices in this letter are: $s_1 = \frac{1}{\sqrt{2}} \begin{pmatrix} 0 & 1 & 0 \\ 1 & 0 & 1 \\ 0 & 1 & 0 \end{pmatrix}$, $s_2 = \frac{1}{\sqrt{2}} \begin{pmatrix} 0 & -i & 0 \\ i & 0 & -i \\ 0 & i & 0 \end{pmatrix}$, $s_3 = \begin{pmatrix} 1 & 0 & 0 \\ 0 & 0 & 0 \\ 0 & 0 & -1 \end{pmatrix}$.
- [29] J. Liu, J. Liu, and X. Dai, Pseudo landau level representation of twisted bilayer graphene: Band topology and implications on the correlated insulating phase, *Phys. Rev. B* **99**, 155415 (2019).
- [30] C. Yuce, Robust bulk states, *Physics Letters A* **383**, 1791 (2019).
- [31] O. Can, T. Tummuru, R. P. Day, I. Elfimov, A. Damascelli, and M. Franz, High-temperature topological superconductivity in twisted double-layer copper oxides, *Nature Physics* **17**, 519–524 (2021).
- [32] J. M. B. Lopes dos Santos, N. M. R. Peres, and A. H. Castro Neto, Graphene bilayer with a twist: Electronic structure, *Phys. Rev. Lett.* **99**, 256802 (2007).
- [33] R. Roy, Band geometry of fractional topological insulators, *Phys. Rev. B* **90**, 165139 (2014).
- [34] F. Xie, Z. Song, B. Lian, and B. A. Bernevig, Topology-bounded superfluid weight in twisted bilayer graphene, *Phys. Rev. Lett.* **124**, 167002 (2020).
- [35] Y. Onishi and L. Fu, Fundamental bound on topological gap (2023), arXiv:2306.00078 [cond-mat.mes-hall].
- [36] G. Grosso and G. Parravicini, *Solid State Physics* (Elsevier Science, 2013).
- [37] D. Ma, Y.-G. Chen, Y. Yu, and X. Luo, Moiré semiconductors on twisted bilayer dice lattice (2023), arXiv:2310.05403 [cond-mat.mes-hall].
- [38] O. Roslyak, G. Gumbs, A. Balassis, and H. Elsayed, Effect of magnetic field and chemical potential on the rkyk interaction in the $\alpha - \text{L}_3$ lattice, *Phys. Rev. B* **103**, 075418 (2021).

Supplemental Materials of Generation of isolated flat bands with tunable numbers through Moiré engineering

THE TIGHT-BINDING MODEL OF THE GENERALIZED LIEB LATTICE

In the basis of $(A, B, C)^T$, the Bloch Hamiltonian with only nearest-neighbor hopping on a Lieb lattice possessing sublattice symmetry is:

$$H_{\text{bulk}}(\vec{k}) = t \begin{pmatrix} 0 & 1 + e^{ik_x} & 0 \\ 1 + e^{-ik_x} & 0 & 1 + e^{ik_y} \\ 0 & 1 + e^{-ik_y} & 0 \end{pmatrix}, \quad (\text{S1})$$

which has a triply degenerated touching at M point and a flat band at $E = 0$. Due to the flat band at $E = 0$, describing the low-energy theory of the Lieb lattice through the continuum model is invalid. Fortunately, this problem can be solved by introducing the second nearest-neighbor hopping into the Lieb lattice. If the second nearest-neighbor hopping t_2 is considered, the Hamiltonian in Eq. S1 becomes:

$$H_{\text{bulk}}(\vec{k}) = t \begin{pmatrix} h & 1 + e^{ik_x} & 0 \\ 1 + e^{-ik_x} & h & 1 + e^{ik_y} \\ 0 & 1 + e^{-ik_y} & h \end{pmatrix}, \quad (\text{S2})$$

where $h = \frac{2t_2}{t}(\cos(k_x) + \cos(k_y))$. With the consideration of the second nearest-neighbor hopping, the flat band disperses, and the band structure develops a valley structure around M point. Then, the low-energy Hamiltonian around M can be described by:

$$H_0(\vec{k}) = t(k_x \lambda_2 + k_y \lambda_7) + t_2 k^2 - 4t_2, \quad (\text{S3})$$

where λ_i is the i^{th} Gell-Mann matrix. Therefore, to rigorously analyze the low-energy theory of the moiré pattern in TBL, we study the low-energy theory in Eq. S3 with $t_2 \rightarrow 0$ and perform calculation results through tight-binding Hamiltonian parameterized by the Slater-Koster method.

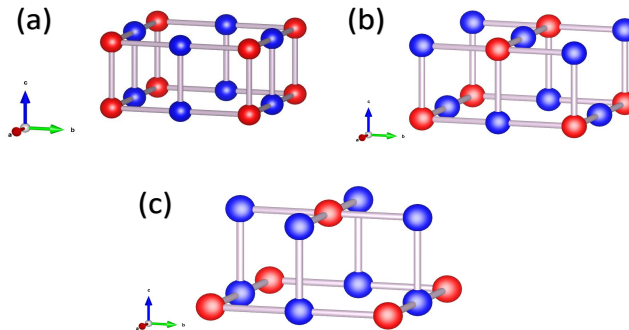


FIG. S1. (a) AA-stacked bilayer Lieb lattice (b) AB_x -stacked bilayer Lieb lattice (c) AB_{xy} -stacked bilayer Lieb lattice

THE TIGHT-BINDING MODEL OF THE GENERALIZED DICE LATTICE

In the basis of $(A, B, C)^T$, the Bloch Hamiltonian with only nearest-neighbor hopping on a Dice lattice possessing sublattice symmetry is [S38]:

$$H_{\text{bulk}}(\vec{k}) = t \begin{pmatrix} 0 & h & 0 \\ h^* & 0 & h \\ 0 & h^* & 0 \end{pmatrix}, \quad (\text{S4})$$

where $h = 1 + 2e^{-i\frac{3k_y}{2}} \cos(\frac{\sqrt{3}k_x}{2})$. Eq. S2 has triply degenerated touching at K, K' points. If the second nearest-neighbor hopping t_2 is considered, the Hamiltonian in Eq. S5 becomes:

$$H_{\text{bulk}}(\vec{k}) = t \begin{pmatrix} h' & h & 0 \\ h^* & h' & h \\ 0 & h^* & h' \end{pmatrix}, \quad (\text{S5})$$

where $h' = \frac{2t_2}{t} (\cos(\frac{\sqrt{3}}{2}k_x + \frac{3}{2}k_y) + \cos(\frac{\sqrt{3}}{2}k_x - \frac{3}{2}k_y) + \cos(\sqrt{3}k_x))$. The low-energy state around the valleys is described by:

$$H_0(\vec{k}) = \frac{3t}{2} (\pm k_x S_1 - k_y S_2) + \frac{9t_2}{4} (k_x^2 + k_y^2), \quad (\text{S6})$$

where S is the spin-1 representation of $SU(2)$.

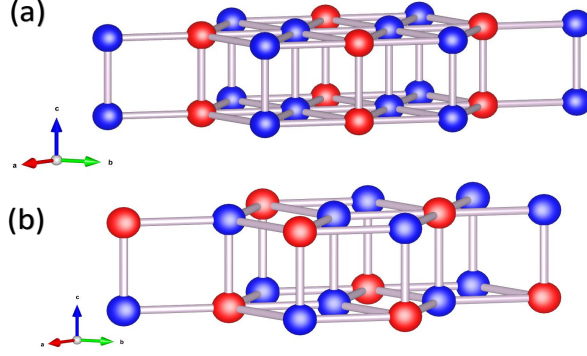


FIG. S2. (a) AA-stacked bilayer Lieb lattice (b) AB-stacked bilayer Lieb lattice

THE TIGHT-BINDING MODEL OF THE TWISTED BILAYERS

We consider AA-stacked twisted bilayer Lieb(Dice) model. For the Lieb structure, any commensurate twist can be described by a so-called 'twist' vector (m, n) . The twist angle is determined by $\theta_{(m,n)} = 2 \arctan(m/n)$ [S31]. The Moire structure can be understood as by rotating two perfectly aligned square lattices in opposite directions by $\theta_{(m,n)}/2$. The Moire unit cell contains $3 \cdot 2(m^2 + n^2)$ atomic sites. The two Moire lattice vectors are

$$\begin{aligned} \mathbf{T}_1 &= \sqrt{(m^2 + n^2)} \mathbf{a}_1 = (\sqrt{(m^2 + n^2)}, 0), \\ \mathbf{T}_2 &= \sqrt{(m^2 + n^2)} \mathbf{a}_2 = (0, \sqrt{(m^2 + n^2)}), \end{aligned} \quad (\text{S7})$$

where $\mathbf{a}_1 = (1, 0)$, $\mathbf{a}_2 = (0, 1)$ are the lattice vectors of the original square lattice. The interlayer spacing is set as 0.8. We choose $(m, n) = (1, 5)$ in this work.

For each constituent layer, we only consider the hopping between nearest neighbour A-B and B-C (the inter-atomic distance is 0.5), and set the hopping parameter $t = 1$. For the interlayer coupling, we truncate the hopping at the cutoff $r=1$, so that the hopping within this range is $t_{int} = 0.2$ while the hopping outside the range is 0. Again, we only consider the hopping A-B and B-C to guaranteed the flatness of the bands.

The commensurate twisted Dice structure can be obtained by rotating the two aligned triangular lattice by $\theta_i/2$ [S32], where

$$\cos(\theta_i) = \frac{3i^2 + 3i + 1/2}{3i^2 + 3i + 1}. \quad (\text{S8})$$

The Moire lattice vectors are

$$\begin{aligned} \mathbf{T}_1 &= i\mathbf{a}_1 + (i+1)\mathbf{a}_2, \\ \mathbf{T}_2 &= -(i+1)\mathbf{a}_1 + (2i+1)\mathbf{a}_2. \end{aligned} \quad (\text{S9})$$

The $\mathbf{a}_1 = 2.46(\sqrt{3}/2, -1/2)$ and $\mathbf{a}_2 = 2.46(\sqrt{3}/2, 1/2)$ are the two lattice vectors of single triangular layer. The interlayer spacing is set as 2. We choose $i=2$ in the calculation.

Similarly as in Lieb structure, for each constituent Dice layer, we only consider the nearest neighbour hopping between A and B, B and C while neglect the hopping between A and C. The intralayer hopping between A and B, B and C is set as 1. For the interlayer coupling, we truncate the hopping at the cutoff $r=2.5$. The hopping within this range is $t_{int} = 0.2$ while the hopping outside the range is 0. Again, we only consider the hopping A-B and B-C to guaranteed the flatness of the bands.

THE PSEUDO-LANDAU LEVELS IN TWISTED BILAYER DICE LATTICE

In the $t_2 = 0$ limit, the low-energy states around the valleys of a Dice lattice monolayer are described by:

$$H_0(\vec{k}) = \frac{3t}{2}(\zeta k_x S_1 - k_y S_2), \quad (\text{S10})$$

where S is the spin-1 representation of $SU(2)$, and $\zeta = \pm$ indicates the valley degree of freedom. On the other hand, the interlayer coupling in Eq. 4 in the main text expanding to the order of $O(\frac{r}{L_s})$ is [S29]:

$$\begin{aligned} T \cong & \omega_2(T_1(1 - i\frac{4\pi y}{3L_s}) + T_2(1 + i\frac{2\pi}{3L_s}(\sqrt{3}x + y)) \\ & + T_3(1 + i\frac{2\pi}{3L_s}(-\sqrt{3}x + y)) + 3\omega_1, \end{aligned} \quad (\text{S11})$$

where $T_n = \cos((n-1)\frac{2\pi}{3})S_1 - \sin((n-1)\frac{2\pi}{3})S_2 + \frac{\omega_3}{\omega_2}(\cos((n-1)\frac{2\pi}{3})\lambda_4 + \sin((n-1)\frac{2\pi}{3})\lambda_5)$. Thus, if we substitute the Hamiltonian in Eq. S10 into Eq. 3 in the main text, Eq. S11 can be treated as the effective vector potential in the twisted bilayer Dice lattice, which is $\vec{A} = -\frac{2\pi\omega_2}{L_s}(\zeta y\hat{x} + x\hat{y})$. The Hamiltonian in Eq. S10 can thus be written as:

$$\begin{aligned} H = & (\frac{3t}{2}\zeta q_x\tau_0 - A_x\tau_3)S_1 - (\frac{3t}{2}q_y\tau_0 - A_y\tau_3)S_2 \\ & - \frac{\omega_3}{\omega_2}(A_x\lambda_4 + A_y\lambda_5)\tau_3 + 3\omega_1\tau_2. \end{aligned} \quad (\text{S12})$$

The third term in Eq. S12 couples the Landau levels within each layer and lifts the degeneracy between different layers, while the fourth term couples the Landau levels in different layers.

In Landau gauge, the effective vector potential is $\vec{A} = \frac{4\pi\omega_2\zeta}{L_s}x\hat{y}$ and the effective field strength $B = \frac{4\pi\omega_2\zeta}{L_s}$. Then, by introducing the creation(annihilation) operator for Landau level $a^\dagger(a) \equiv \frac{1}{\sqrt{2\hbar eB}}(\pi_x \pm i\pi_y)$ with the canonical momentum $\vec{\pi} \equiv \vec{k} - e\vec{A}$, the Hamiltonian in Eq. S12 in the chiral limit $\omega_1 = \omega_3 = 0$ can be rewritten as:

$$H = \hbar\omega_c \begin{pmatrix} 0 & a^\dagger & 0 \\ a & 0 & a^\dagger \\ 0 & a & 0 \end{pmatrix}, \quad (\text{S13})$$

where the cyclotron frequency $\omega_c = \frac{3t}{2}\sqrt{\frac{2eB}{\hbar}}$. To solve for the Landau level, we assume the eigenstate of the n^{th} Landau level $|\psi_n(k)\rangle$ with eigenvalue E_n consists of:

$$|\psi_n(k)\rangle = \frac{e^{ikx}}{\sqrt{2L_x l_B}}(u_n \begin{pmatrix} 1 \\ 0 \\ 0 \end{pmatrix} |n+1\rangle + v_n \begin{pmatrix} 1 \\ 1 \\ 0 \end{pmatrix} |n\rangle + w_n \begin{pmatrix} 0 \\ 0 \\ 1 \end{pmatrix} |n-1\rangle), \quad (\text{S14})$$

where u_n , v_n , and w_n are some complex numbers. Here, the magnetic length $l_B = \sqrt{\frac{3L_s\hbar t}{8\pi\omega_2}}$ and the L_x is the system's size in the \hat{x} -direction. The eigenstate of the cyclotron motion $|n\rangle$ satisfies $a|n\rangle = \sqrt{n}|n-1\rangle$ and $a^\dagger|n\rangle = \sqrt{n+1}|n+1\rangle$. Then, according to the eigenvalue equation $H|\psi_n(k)\rangle = E_n|\psi_n(k)\rangle$, E_n satisfies:

$$\det \begin{pmatrix} E_n & -\hbar\omega_c\sqrt{n+1} & 0 \\ -\hbar\omega_c\sqrt{n+1} & E_n & -\hbar\omega_c\sqrt{n} \\ 0 & -\hbar\omega_c\sqrt{n} & E_n \end{pmatrix} = 0. \quad (\text{S15})$$

Eq. S15 has the solution:

$$E_n = 0 \quad \text{or} \quad E_n = \lambda \hbar \omega_c \sqrt{2n+1} \quad \forall n \in \mathbb{N}, \quad (\text{S16})$$

leading to a large degeneracy of the zero modes, i.e., $\frac{1}{3}$ positive integer Landau levels are zero modes. In the following, we absorb the index k and the prefactor $\frac{e^{ikx}}{\sqrt{2L_x L_B}}$ into our bracket notation for our convenience. Here, $\lambda = \pm 1$. The corresponding eigenmodes are:

$$\begin{aligned} |0n\rangle &= \frac{1}{\sqrt{2n+1}} \begin{pmatrix} \sqrt{n}|n+1\rangle \\ 0|n\rangle \\ -\sqrt{n+1}|n-1\rangle \end{pmatrix} \\ |\lambda n\rangle &= \frac{\lambda}{\sqrt{4n+2}} \begin{pmatrix} \sqrt{n+1}|n+1\rangle \\ \lambda\sqrt{2n+1}|n\rangle \\ \sqrt{n}|n-1\rangle \end{pmatrix}. \end{aligned} \quad (\text{S17})$$

Then, to calculate the Hall conductivity of these Landau levels, we need to first calculate the matrix elements for the velocity operators:

$$\begin{aligned} \langle 0n' | \hat{S}_1 | 0n \rangle &= 0 \\ \langle 0n' | \hat{S}_1 | \lambda n \rangle &= \frac{1}{\sqrt{4n'+2}} (\sqrt{n'} \delta_{n'+1,n} - \sqrt{n'+1} \delta_{n'-1,n}) \\ \langle \lambda' n' | \hat{S}_1 | \lambda n \rangle &= \frac{\lambda \lambda'}{2\sqrt{2n+1}\sqrt{2n'+1}} (\lambda \sqrt{n'+1} \sqrt{2n+1} \delta_{n'+1,n} \\ &\quad + \lambda' \sqrt{2n'+1} (\sqrt{n+1} \delta_{n',n+1} + \sqrt{n} \delta_{n',n-1}) \\ &\quad + \lambda \sqrt{n'} \sqrt{2n+1} \delta_{n'-1,n}) \\ \langle 0n' | \hat{S}_2 | 0n \rangle &= 0 \\ \langle 0n' | \hat{S}_2 | \lambda n \rangle &= \frac{-i}{\sqrt{4n'+2}} (\sqrt{n'} \delta_{n'+1,n} + \sqrt{n'+1} \delta_{n'-1,n}) \\ \langle \lambda' n' | \hat{S}_2 | \lambda n \rangle &= \frac{i \lambda \lambda'}{2\sqrt{2n+1}\sqrt{2n'+1}} (-\lambda \sqrt{2n+1} \sqrt{n'+1} \delta_{n'+1,n} \\ &\quad + \lambda' \sqrt{2n'+1} (\sqrt{n+1} \delta_{n',n+1} - \sqrt{n} \delta_{n',n-1}) \\ &\quad + \lambda \sqrt{2n+1} \sqrt{n'} \delta_{n'-1,n}) \end{aligned}$$

The Hall conductivity is calculated by [S29]:

$$\sigma(\mu) = \frac{\eta_0 e^2}{h} \sum_{kk', N \neq N', \xi \xi'} \left(\frac{f(E_{N\xi k} - \mu) - f(E_{N'\xi' k'} - \mu)}{(E_{N\xi k} - E_{N'\xi' k'})^2} \times \text{Im}(\langle N\xi k | \hat{v}_x | N'\xi' k' \rangle \langle N'\xi' k' | \hat{v}_y | N\xi k \rangle) \right) \quad (\text{S18})$$

where $\xi = \pm 1$ or 0 , $\eta_0 = -\frac{2\pi\hbar^2}{L_x L_y}$, and $f(E - \mu)$ is the Fermi-Dirac distribution at chemical potential at μ . The Hall conductivity can be rewritten into a form that is more convenient for calculation:

$$\sigma(\mu) = \sigma(\mu)_{\xi=0, \xi'=\lambda} + \sigma(\mu)_{\xi=\lambda, \xi'=0} + \sigma(\mu)_{\xi=\lambda, \xi'=\lambda'}, \quad (\text{S19})$$

where $\lambda, \lambda' = \pm 1$. Here,

$$\begin{aligned} \sigma(\mu)_{\xi=0, \xi'=\lambda} &= \frac{\eta_0 e^2}{h} \sum_{kk', N \neq N', 0\lambda} \left(\frac{f(-\mu) - f(\lambda \hbar \omega_c \sqrt{2N'+1} - \mu)}{\hbar^2 \omega_c^2 (2N'+1)} \times \text{Im}(\langle N0k | \hat{v}_x | N'\lambda k' \rangle \langle N'\lambda k' | \hat{v}_y | N0k \rangle) \right) \\ \sigma(\mu)_{\xi=\lambda, \xi'=0} &= \frac{\eta_0 e^2}{h} \sum_{kk', N \neq N', \lambda 0} \left(\frac{f(\lambda \hbar \omega_c \sqrt{2N+1} - \mu) - f(-\mu)}{\hbar^2 \omega_c^2 (2N+1)} \times \text{Im}(\langle N\lambda k | \hat{v}_x | N'0k' \rangle \langle N'0k' | \hat{v}_y | N\lambda k \rangle) \right) \\ \sigma(\mu)_{\xi=\lambda, \xi'=\lambda'} &= \frac{\eta_0 e^2}{h} \sum_{kk', N \neq N', \lambda \lambda'} \left(\frac{f(\lambda \hbar \omega_c \sqrt{2N+1} - \mu) - f(\lambda' \hbar \omega_c \sqrt{2N'+1} - \mu)}{\hbar^2 \omega_c^2 (\lambda \sqrt{2N+1} - \lambda' \sqrt{2N'+1})^2} \times \text{Im}(\langle N\lambda k | \hat{v}_x | N'\lambda' k' \rangle \langle N'\lambda' k' | \hat{v}_y | N\lambda k \rangle) \right), \end{aligned} \quad (\text{S20})$$

respectively. Since $\hat{v}_i = v_i \hat{S}_i$, Eq. S20 becomes:

$$\begin{aligned}
\sigma(\mu)_{\xi=0, \xi'=\lambda} &= \frac{\eta_0 e^2}{h} \sum_{k, N \neq N', \lambda} \left(\frac{f(-\mu) - f(\lambda \hbar \omega_c \sqrt{2N'+1} - \mu)}{\hbar^2 \omega_c^2 (2N'+1)} \times \left(\frac{v_1 v_2}{4N'+2} (N \delta_{N+1, N'} - (N+1) \delta_{N-1, N'}) \right) \right) \\
\sigma(\mu)_{\xi=\lambda, \xi'=0} &= \frac{\eta_0 e^2}{h} \sum_{k, N \neq N', \lambda} \left(\frac{f(-\mu) - f(\lambda \hbar \omega_c \sqrt{2N+1} - \mu)}{\hbar^2 \omega_c^2 (2N+1)} \times \left(\frac{v_1 v_2}{4N'+2} (N' \delta_{N'+1, N} - (N'+1) \delta_{N'-1, N}) \right) \right) \\
\sigma(\mu)_{\xi=\lambda, \xi'=\lambda'} &= \frac{\eta_0 e^2}{h} \sum_{k, N \neq N', \lambda} \left(\frac{f(\lambda \hbar \omega_c \sqrt{2N+1} - \mu) - f(-\lambda \hbar \omega_c \sqrt{2N'+1} - \mu)}{\hbar^2 \omega_c^2 (\sqrt{2N+1} + \sqrt{2N'+1})^2} \times \frac{v_1 v_2}{4(2N+1)(2N'+1)} \right) \\
&\quad \times ((-N'+1)(2N+1) \delta_{N'+1, N} + (2N'+1)((N+1) \delta_{N', N+1} - N \delta_{N', N-1}) + N'(2N+1) \delta_{N'-1, N}) \\
&= 0.
\end{aligned} \tag{S21}$$

Then, by using the expression in Eq. S21, we can rewrite Eq. S19 into:

$$\begin{aligned}
\sigma(\mu) &= \frac{v_1 v_2}{\hbar^2 \omega_c^2} \frac{2\eta_0 e^2}{h} \sum_{k, N \neq N', \lambda} (f(-\mu) - f(\lambda \hbar \omega_c \sqrt{2N+3} - \mu)) \frac{1}{4N+2} \frac{N}{2N+3} \\
&\quad - (f(-\mu) - f(\lambda \hbar \omega_c \sqrt{2N+1} - \mu)) \frac{1}{2N+1} \frac{N+2}{4N+6} \\
&= \begin{cases} -\frac{e^2}{3h} & , \text{ if } 0 < \mu < \hbar \omega_c \\ \frac{e^2}{3h} & , \text{ if } -\hbar \omega_c < \mu < 0 \end{cases}.
\end{aligned} \tag{S22}$$

Note that Eq. S22 is the Hall conductivity contributed only from $n \in \mathbb{N}$ Landau levels. To have the total Hall conductivity, we need to consider the contribution from $n = 0$ Landau levels:

$$\begin{cases} |0, n=0\rangle = (|0\rangle \ 0 \ 0)^T & , \text{ with } E_{n=0} = 0 \\ |\lambda, n=0\rangle = \frac{1}{\sqrt{2}} (|1\rangle \ \lambda|0\rangle \ 0)^T & , \text{ with } E_{n=0, \lambda} = \lambda \hbar \omega_c. \end{cases} \tag{S23}$$

The only non-vanishing matrix elements of the velocity operators that involve $n = 0$ Landau levels are:

$$\begin{aligned}
\langle 0, 0 | \hat{S}_{1(2)} | \lambda, 0 \rangle &= (-i) \frac{\lambda}{\sqrt{2}} \\
\langle \lambda', 0 | \hat{S}_{1(2)} | \lambda, 1 \rangle &= (-i) \left(\frac{1}{2} + \frac{\lambda \lambda'}{\sqrt{12}} \right) \\
\langle \lambda', 0 | \hat{S}_{1(2)} | 0, 1 \rangle &= (-i) \frac{-\lambda'}{\sqrt{3}}
\end{aligned} \tag{S24}$$

The corresponding contribution to the Hall conductivity is calculated by:

$$\begin{aligned}
\sigma(\mu) &= \frac{\eta_0 e^2}{h} \frac{v_1 v_2}{\hbar^2 \omega_c^2} \sum_{k, N \neq N', \lambda, \lambda'} (f(-\mu) - f(\lambda \hbar \omega_c - \mu)) \delta_{\lambda \lambda'} + (f(\lambda' \hbar \omega_c - \mu) - f(\lambda \hbar \omega_c - \mu)) \left(\frac{1}{2} + \frac{\lambda \lambda'}{\sqrt{3}} + \frac{1}{6} \right) \\
&\quad + (f(\lambda' \hbar \omega_c - \mu) - f(-\mu)) \frac{2}{3} \delta_{\lambda \lambda'} \\
&= \begin{cases} \frac{e^2}{3h} & , \text{ if } 0 < \mu < \hbar \omega_c \\ -\frac{e^2}{3h} & , \text{ if } -\hbar \omega_c < \mu < 0 \end{cases}.
\end{aligned} \tag{S25}$$

Therefore, combining Eq. S22 and Eq. S25, the total Hall conductivity contributed from all Landau levels is:

$$\sigma_{\text{tot}}(\mu) = \begin{cases} 0 & , \text{ if } 0 < \mu < \hbar \omega_c \\ 0 & , \text{ if } -\hbar \omega_c < \mu < 0 \end{cases}. \tag{S26}$$

Therefore, the Chern number of all the zero-mode Landau levels is $C = 0$.

If the magnetic field is along the $-\hat{z}$ direction, the Hamiltonian in Eq. S13 becomes:

$$H = \hbar\omega_c \begin{pmatrix} 0 & a & 0 \\ a^\dagger & 0 & a \\ 0 & a^\dagger & 0 \end{pmatrix}, \quad (\text{S27})$$

and the corresponding eigenmodes are:

$$\begin{aligned} |0n\rangle &= \frac{1}{\sqrt{2n+1}} \begin{pmatrix} -\sqrt{n+1}|n-1\rangle \\ 0|n\rangle \\ \sqrt{n}|n+1\rangle \end{pmatrix} \\ |\lambda n\rangle &= \frac{\lambda}{\sqrt{4n+2}} \begin{pmatrix} \sqrt{n}|n-1\rangle \\ \lambda\sqrt{2n+1}|n\rangle \\ \sqrt{n+1}|n+1\rangle \end{pmatrix} \\ |0, n=0\rangle &= \begin{pmatrix} 0 \\ 0 \\ |0\rangle \end{pmatrix}, \quad |\lambda, n=0\rangle = \frac{1}{\sqrt{2}} \begin{pmatrix} 0 \\ \lambda|0\rangle \\ |1\rangle \end{pmatrix} \end{aligned} \quad (\text{S28})$$

The matrix elements of the velocity operators \hat{v}_y flip a sign compared to the system with a magnetic field in the \hat{z} direction. Thus, the Hall conductivity of the zero-mode Landau levels differs by a minus sign from the one under a magnetic field in the \hat{z} direction.